Continuity waves in resolved-particle simulations of fluidized beds

Daniel P. Willen,[1,*] Adam J. Sierakowski,[1,†] Gedi Zhou,[1,‡] and Andrea Prosperetti[2,3,§]

[1]*Department of Mechanical Engineering, Johns Hopkins University, 3400 North Charles Street, Baltimore, Maryland 21218, USA*

[2]*Department of Mechanical Engineering, University of Houston, 4726 Calhoun Rd, Houston, Texas 77204-4006, USA*

[3]*Faculty of Science and Technology and J. M. Burgers Centre for Fluid Dynamics, University of Twente, P.O. Box 217, 7500 AE Enschede, the Netherlands*

The results of a fully resolved simulation of up to 2000 spheres suspended in a vertical liquid stream are analyzed by a method based on a truncated Fourier series expansion. It is shown that, in this way, it is possible to identify continuity (or kinematic) waves and to determine their velocity, which is found to closely agree with the theory of one-dimensional continuity waves based on the Richardson-Zaki drag correlation.

I. INTRODUCTION

Kinematic (or continuity, or density) waves are among the simplest form of nonlinear waves [1] and are widely encountered in many areas such as traffic flow, avalanches, suspensions, and many others. The denomination arises from the fact that the flux of some conserved quantity is expressed directly in terms of that quantity, thus bypassing the need for the consideration of dynamic effects. In these conditions the statement of continuity, complemented by suitable boundary and initial conditions, is sufficient to completely determine the evolution of the conserved quantity in space and time.

In this paper we describe fully resolved simulations of a fluidized-bedlike solid-liquid system and show how the results can be analyzed so as to bring out the existence of kinematic waves and calculate their velocity. It is found that the velocity calculated in this way is in very good agreement with existing estimates based on a macroscopic, averaged formulation of fluidized beds [2]. An additional element of interest of this work is the description of a method by which detailed, microscopic information on a complex fluid-particle system can be interrogated to extract information that concerns the average, macroscopic character of the system.

In a fluidized bed particles (or droplets) become suspended in an upward-directed fluid stream once the flow velocity exceeds the so-called minimum fluidization velocity (see, e.g., Ref. [3]). As the velocity increases further, the mean particle density decreases until, when the flow velocity becomes comparable to the single-particle terminal settling velocity, they are blown out of the system. Fluidized beds find major applications in chemical engineering, the oil industry, combustion, and other areas because of the intimate contact that they promote between the solid and fluid phases.

The efficiency of these and other types of fluidized beds would be higher were it not for the fact that the particle-fluid mixture does not remain homogeneous. Rising regions of low particle density, referred to as "bubbles," very frequently form, particularly when there is a large density difference between the particles and the fluid, such as in a gas-solid fluidized bed. The precise mechanism producing these structures has been debated for decades, but firm conclusions resulting from these

---

*daniel.willen@jhu.edu; www.physaliscfd.org

†sierakowski@jhu.edu

‡gedi.zhou@gmail.com

§aprosper@central.uh.edu

114305-1

efforts are disappointingly few. A widely held belief is that bubbles form as the result of a cascade of instabilities, the first one of which affects the initial uniform state of fluidization which loses stability to vertically propagating density waves [4–14]. This is one of the reasons of interest in the study of kinematic waves in disperse fluid-particle systems. Besides fluidized beds, other particulate systems display density waves, as first recognized by Kynch in the study of settling suspensions, and further elaborated in later studies by others [2,15,16].

Nearly all existing theoretical studies of kinematic waves in particulate systems are based on coarse-grained descriptions in which the particles are modeled in an average sense. The only exception is Ref. [17] in which lattice-Boltzmann simulations for conditions close to those of the experiments of Ref. [18] are described. In order to limit the complexity of the horizontal structure of the voidage waves the authors used domains with a very small horizontal extent, mostly $12a \times 12a$, with a the particle radius, finding a generally good match with the experiments of Refs. [7,18]. They noticed the presence of voidage waves but did not attempt to interpret them as kinematic waves.

II. COMPUTATIONAL METHODS

Recent improvements in computational capabilities and numerical methods have rendered possible the simulation of thousands of fully resolved particles, giving unprecedented access to detailed information on the flow in the neighborhood of each particle and on the particles response. In this study we take advantage of these developments and show how this detailed particle-level information can be processed to identify the presence of kinematic waves. We compare the celerity of these waves with the theory developed in earlier averaged treatments and find a very good agreement between the two.

The simulations are performed with the Physalis method, a complete description of which is available in several papers including, most recently, Ref. [19]; implementation details are described in Ref. [20]. The Navier-Stokes equations are solved on a fixed Cartesian grid by a projection method. A characteristic feature of the method is the way in which the fluid is coupled to the particles, assumed to be rigid spheres. The coupling is based on the recognition that, in the vicinity of the no-slip particle surfaces, the fluid motion differs little from a rigid-body motion. This circumstance permits the Navier-Stokes equations to be linearized to the Stokes form, for which an exact solution, obtained by Lamb [21,22], is available. This analytical solution is used as a "bridge" between the particle surface and the closest nodes of the Cartesian grid, thus bypassing the difficulties deriving from the complex geometrical relationship between the spherical particles and the underlying Cartesian grid. The particle position and orientation is updated on the basis of the calculated forces and couples of hydrodynamic origin, collisions, gravity, and buoyancy.

The method, which has been extensively validated in earlier papers (see, e.g., Refs. [19,23]), is accurate and efficient. Since the Lamb solution is expressed as a series of spherical harmonics, the error decreases exponentially, rather than algebraically, with the increase of the number of degrees of freedom used to describe each particle. This feature is in marked contrast with the algebraic error decrease of most other methods, such as immersed-boundary. The forces and couples on the particles are given directly from the coefficients of the expansion with no need for additional calculation. The no-slip condition at the particle surface is satisfied to analytical accuracy whatever the level of truncation of the series in the Lamb solution.

Simulations

The computational domain used in the present simulations was triply periodic with a square cross section of dimension $20a \times 20a$ and a vertical extent of $60a$; all particles were assumed to have equal radius. We used eight mesh lengths per particle radius, which, on the basis of our previous experience, provides a very good accuracy in the range of Reynolds number relevant for this study. By balancing the gravitational forcing in the vertical direction with an imposed upward pressure gradient, the simulations were in effect carried out in a reference frame coincident with the mean

TABLE I. Values of the parameters used in the collision model of Ref. [19]

Young's modulus, E (MPa)	0.65
Poisson ratio, σ	0.5
Dry coefficient of restitution, e_{dry}	0.98
Coefficient of friction, μ_f	0.5

vertical particle motion. With 500, 1000, 1500, and 2000 equal particles the mean particle volume fraction ϕ took the values 0.087, 0.175, 0.262, 0.349, respectively. We considered four different values of the particle-to-fluid density ratio, $\rho^* \equiv \rho_p/\rho_f = 2.0, 3.3, 4.0, 5.0$.

The parameters for the simulations were chosen to match experiments by Richardson and Zaki [24], who used glass spheres of radius 2.1 mm; our simulations for $\rho^* = 3.3$ correspond to the liquid with density $\rho_f = 875$ kg/m^3 and kinematic viscosity $\nu_f = 1.715 \times 10^{-5}$ m^2/s that they denote by $R_0 I$. Details of the model are described in Ref. [19]. With the exception of Young's modulus, which is softened for numerical reasons as explained in Ref. [19], the physical parameters used in the particle collision model, listed in Table I, were chosen to match those of glass spheres. The collision Stokes number $\text{St}_c = \rho^* \text{Re}_r/9$, with Re_r the particle Reynolds number based on the relative velocity, characterizes the strength of collisions (see, e.g., Ref. [25]). Typical values of St_c encountered in the present simulations were at most 10–20. Thus, collisions are dominated by the fluid viscosity and are too weak to result in a rebounding motion of the colliding particles (see Fig. 6 in Ref. [19]). For this reason, the use of a smaller Young's modulus cannot affect the results in any significant way.

In order to characterize the balance between gravity and viscous dissipation it is convenient to use the Galilei number

$$\text{Ga} = \frac{1}{\nu} \sqrt{\left(\frac{\rho_p}{\rho_f} - 1\right)(2a)^3 g}, \tag{1}$$

in which g is the acceleration of gravity and ν the fluid kinematic viscosity; the values of Ga corresponding to the present simulations are shown in Table II. By carrying out separate simulations in domains with size $20a \times 20a \times 80a$ we have calculated the terminal settling velocity w_t of single particles for the density ratios used in this study. The results, together with the corresponding single-particle Reynolds number $\text{Re}_t = 2aw_t/\nu$, are also shown in Table II together with a measurement reported in Ref. [24] and an empirical relation valid for $20 < \text{Re}_t < 260$ [26]:

$$\text{Ga}^2 = 18\text{Re}_t \left[1 + 0.1935\text{Re}_t^{0.6305}\right]. \tag{2}$$

TABLE II. Galilei number, single-particle terminal velocity w_t, and corresponding Reynolds number for the present simulations compared with an experimental result from Ref. [24] (R&Z) and simulations from Ref. [26] (Y&K).

| ρ_p/ρ_f | Current work | | | R&Z | Y&K |
	Ga	w_t m/s	Re_t	w_t m/s, Re_t	Re_t
2.0	49.7	0.177	43.27	–	44.17
3.3	75.4	0.313	76.60	0.319, 78.25	78.40
4.0	86.1	0.374	91.57	–	93.82
5.0	99.4	0.453	110.84	–	113.74

There is a good agreement between our single-particle simulations, the experimental data point and the empirical relation (2) with maximum differences of less than 3%. Similar differences were found in an earlier paper [19] and shown to be comparable with those of other recent numerical studies.

Particles were initially randomly arranged in the computational domain and, before data were recorded, allowed to reach a statistically steady state as revealed by the average values of the fluid velocity and particle velocity fluctuations. For the lower densities and volume fractions we could run the simulations used to calculate the speed of kinematic waves for dimensionless times $\nu t/(2a)^2$ up to 24.3. However, as the density ratio and volume fraction increase, interparticle interactions become more frequent and energetic, which requires a smaller time step and more iterations for convergence. In these cases, for practical reasons, we only integrated up to $\nu t/(2a)^2$ of about 14.2. The integration time necessary for the comparisons with the Richardson-Zaki correlation was significantly shorter [in some cases as short as $\nu t/(2a)^2 = 0.7$] since the fluid velocity did not take much time to reach steady state. Due to computational constraints, we were unable to run simulations with larger density ratios and volume fractions for long enough to calculate the kinematic wave speed. These simulations were, however, included in the comparison to the Richardson-Zaki correlation.

III. KINEMATIC WAVES

When the particle density is not too different from that of the fluid, in steady conditions dynamical effects are minor and the particle velocity is mostly determined by the hindrance that they provide to each other's motion and to the motion of the fluid in the interstitial spaces. In these conditions the primary determinant of the particle-fluid relative velocity is the particle volume fraction as has been known since the early days of studies on this subject. A one-dimensional balance equation for the particle volume fraction may be written in the form

$$\frac{\partial \phi}{\partial t} + \frac{\partial j_p}{\partial z} = 0, \tag{3}$$

where j_p is the flux of the volume fraction ϕ and z the vertical coordinate directed upward; t is time. In the conditions envisaged here the particle flux can be expressed in terms of the volume fraction ϕ. Application of the chain rule to the second term of (3) then results in a first-order wave equation in which the speed c with which information about volume fraction changes propagates is given by $c = dj_p/d\phi$.

Richardson-Zaki correlation

The particle flux j_p can be expressed as the sum of a component ϕj, describing the fact that the particles travel with the mixture volume flux j, and a drift-flux component j_d, which corrects for the difference between j and the actual particle flux. If the particles and fluid mean velocities are denoted by $\langle w_p \rangle$ and $\langle w_f \rangle$, we have $j = \phi \langle w_p \rangle + (1 - \phi)\langle w_f \rangle$, and the particle flux relative to j is $j_d = \phi(j - \langle w_p \rangle) = \phi(1 - \phi)(\langle w_p \rangle - \langle w_f \rangle)$. A well-known empirical relationship for $\langle w_p \rangle - \langle w_f \rangle$ was developed by Richardson and Zaki [24] in the form

$$\frac{\langle w_f \rangle - \langle w_p \rangle}{w_t} = \kappa(1 - \phi)^{n-1}, \tag{4}$$

where the exponent n depends on the single-particle Reynolds number; a correlation describing this dependence is $(5.1 - n)/(n - 2.7) = 0.1\mathrm{Re}_t^{0.9}$ [27]. The parameter κ in Eq. (4) is a slowly decreasing function of Re_t and is somewhat less than 1 [26,28–31]. This circumstance reflects the fact that the mutual interference among the particles, mostly due to their slowly decaying wakes, persists even in very dilute systems; a similar effect is found in the case of rising bubble swarms [32,33].

We can calculate $\langle w_f \rangle$ and $\langle w_p \rangle$ from our numerical results by carrying out volume and time averages over the entire computational domain and duration of the simulations and fit a relation of the form (4) to the results, thus determining values for κ and n. The computed values are given in Table III and shown in graphical form in Fig. 1, where they are compared with the results of Ref. [26]

TABLE III. Fitted parameters κ and n from the current simulations with 95% confidence intervals.

Re_t	n	κ
43.27	3.25 ± 0.15	0.87 ± 0.04
76.60	3.03 ± 0.11	0.85 ± 0.03
91.57	2.94 ± 0.11	0.84 ± 0.03
110.84	2.94 ± 0.08	0.85 ± 0.02

for κ and Refs. [24] (solid line) and [27] (dashed line) for n. Figure 2 compares the present simulation results for the mean liquid-particle relative velocity (symbols) with the Richardson-Zaki curve (4) (lines) calculated with the parameter values derived from the present simulations. These comparisons are very favorable, which provides additional confidence in the present numerical results.

Upon making use of (4) in the expression for the particle volume flux we find

$$j_p = \phi j - \kappa w_t \phi (1 - \phi)^n, \tag{5}$$

from which, upon differentiation with respect to ϕ and recognizing the fact that the total flux j is a constant [as follows immediately by adding (3) to its counterpart written for the liquid volume fraction $1 - \phi$], we find

$$c = j - \kappa w_t (1 - \phi)^{n-1} [1 - (n + 1)\phi]. \tag{6}$$

In the situation considered here the mean particle velocity vanishes so that $j = (1 - \phi)\langle w_f \rangle$. Use of (4) then gives the well-known result (see, e.g., Ref. [2], p. 189)

$$c = \kappa n \phi (1 - \phi)^{n-1} w_t. \tag{7}$$

A point worthy of explicit notice is that, according to kinematic wave theory, the waves are nondispersive. Dispersive effects may exist of course, but they will be small in situations in which kinematic wave theory is approximately applicable. A quantification of dispersion would require a coupling of the continuity and momentum equations and, therefore, a more sophisticated theory.

IV. KINEMATIC WAVE SPEED

In a system seat of waves, all the fields will exhibit a wave structure that propagates with the same velocity. In order to determine this velocity we make use of the autocorrelation of the fields on the basis of the following argument. Consider a generic field f, such as the particle number density, volume fraction or other. Since the system under consideration is statistically uniform over horizontal
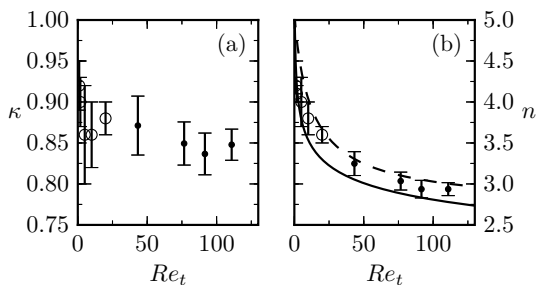

FIG. 1. Comparison of the power-law fit coefficients n and κ in Eq. (4). Black dots are from this study, white circles are from Ref. [26], and the solid and dashed lines are relations for n from Refs. [24,27], respectively.
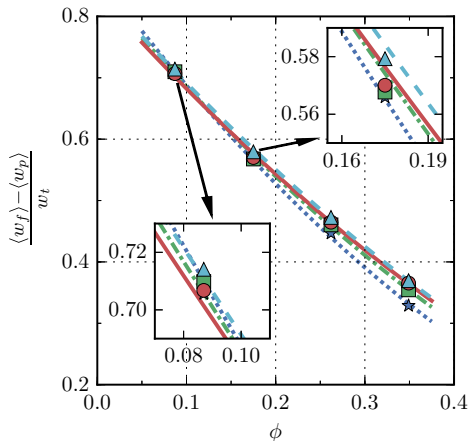
FIG. 2. Comparison of the present simulation results for the mean fluid-particle relative velocity (symbols) with the Richardson-Zaki curve (4) (lines). The dotted line and stars are for $\rho_p/\rho = 2$; the dash-dotted line and green squares for $\rho_p/\rho = 3.3$; the solid line and red circles for $\rho_p/\rho = 4$; and the dashed line and light blue triangles for $\rho_p/\rho = 5$. Insets: top right: close-up of $\phi \approx 0.175$; bottom left: close-up of $\phi \approx 0.087$.

planes we will consider fields averaged over the horizontal variables x and y and dependent only on the vertical coordinate z and time.

A pure wave propagating in the z direction would confer to the field f a space and time dependence of the form $f(z,t) = f(z - ct)$. The space-time autocorrelation is $f(z + \Delta z, t + \Delta t) f(z,t) = f[z + \Delta z - c(t + \Delta t)] f(z - ct)$ and, for $\Delta z = c \Delta t$, it reduces to $f^2(z,t)$ and exhibits therefore a maximum. In the present system the waves are contaminated by the randomness of the particle distribution. In order to bring out this maximum with greater clarity we average the autocorrelation over z, since the system is statistically homogeneous in the vertical direction, and over time, since we consider only the numerical results at steady state after the initial transient has faded away. Thus we focus on quantities of the type

$$R_{ff}(\Delta z, \Delta t) = \langle f(z + \Delta z, t + \Delta t) f(z,t) \rangle, \tag{8}$$

where angle brackets denote the space-time average, and, for brevity, we write f in place of $(f - \langle f \rangle)/\sqrt{\sigma_f}$, with σ_f the variance of f so that, in fact, R_{ff} denotes the autocorrelation function of f. In the presence of waves this quantity will exhibit a series of maxima along lines $\Delta z = c(\Delta t + NT)$ with T the wave period, $N = 0$ for the first wave, $N = 1$ for the second one, and so on. From the slope of these lines in a $\Delta t, \Delta z$ plane we can then determine the wave speed c. Again, because of the statistical irregularities of the system, we might well expect that the line of maxima will be strongest for the first wave and gradually decay as the value of f at a certain position z_0 cannot be expected to be very strongly correlated to the value of f at the same position several waves later. Similarly, the value of f at a certain time t_0 cannot be expected to be strongly correlated to its value at the same instant several wavelengths away.

With the present numerical data, a naive way to implement this approach is to calculate averages of the field of interest over horizontal layers of cells thus generating a discretized version of $f(z,t)$; we will use the adjective "raw" to refer to quantities obtained in this way. As an example, a snapshot of the "raw" particle number density n so calculated is shown by the thin dashed line in Fig. 3 for the case $\rho_p/\rho = 3.3$ with 1000 particles (the quantity shown is vn, the particle number density normalized by the sphere volume $v = \frac{4}{3}\pi a^3$). Each data point is calculated by counting the particle centers contained in a single horizontal layer of cells and dividing by the volume of the layer. It is evident that, even after this horizontal averaging, the result is affected by a considerable amount of noise. Figure 4 shows the autocorrelation function R_{nn} for these parameter values calculated
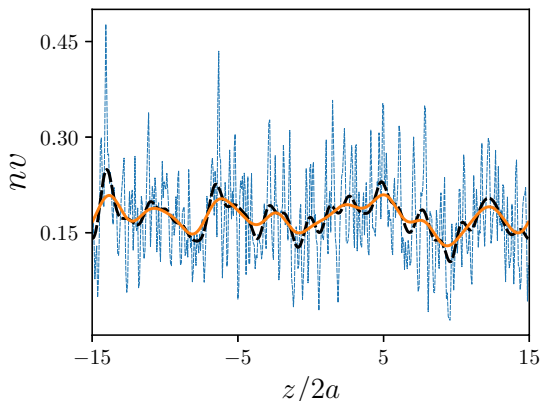
FIG. 3. The thin dashed line is a snapshot of the "raw" number density, i.e., the number density calculated by counting the particle centers contained in each horizontal layer of cells, for $\rho_p/\rho = 3.3$ with 1000. The solid line and the thick dashed line are the number density reconstructed by a Fourier series with 15 and 30 coefficients, respectively.

as explained before by averaging over z and t. While approximately parallel lines of maxima and minima are vaguely suggested by this figure, a strong signal can be identified only for the first wave and only for very small values of Δz and Δt. It would be very difficult to deduce a precise estimation of the wave speed from results of this type.

The situation is very similar if we try to use other fields. In principle the particle volume fraction can be calculated by counting the fraction of the volume of each horizontal layer of cells falling inside particles. A snapshot of the particle volume fraction obtained in this way versus z similar to that of Fig. 3 is shown by the dashed line in Fig. 5. A number of peaks with a width of about 1 can be discerned which, given the normalization in terms of the particle diameter, evidently correspond to fluctuations on the scale of single particles. The autocorrelation function of the volume fraction so calculated (averaged over z and t) is shown in Fig. 6. Once again we can distinguish a series of inclined linelike features, but we encounter the same problem as before if we are interested in an accurate determination of c.
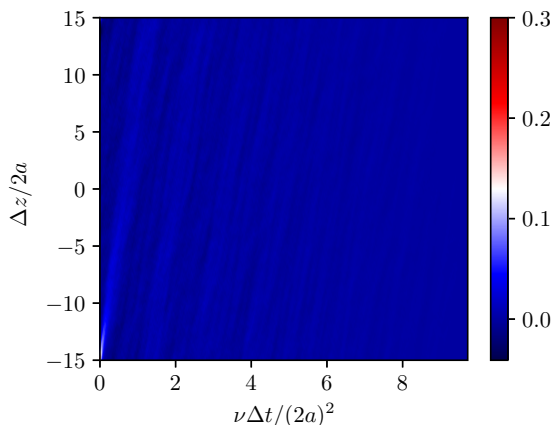

FIG. 4. Autocorrelation function (averaged over horizontal planes and z and t) of the "raw" particle number density, i.e., the number density calculated by counting the particle centers contained in each horizontal layer of cells, for $\rho_p/\rho = 3.3$ with 1000 particles.
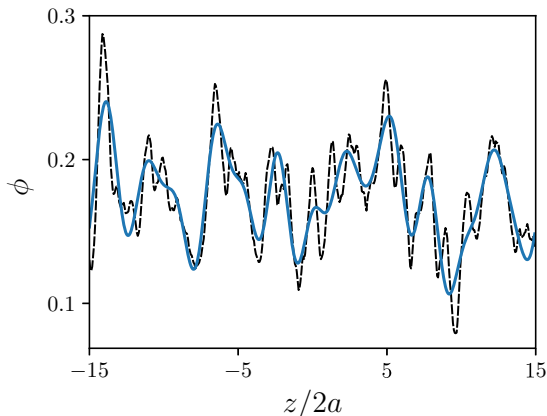
FIG. 5. The dashed line is the "raw" particle volume fraction, i.e., the volume fraction calculated as the fraction of volume of each horizontal cell layer falling inside particles for $\rho_p/\rho = 3.3$ with 1000 particles. The solid line is the particle volume fraction reconstructed by a Fourier series with 15 coefficients.

The use of additional short-time or short-space averaging might perhaps reduce the influence of statistical fluctuations, but it would make it more difficult to discern the space-time variability associated with the waves by blurring their distinct spatio-temporal structure. The challenge facing this procedure is illustrated by the space-time representation of the "raw" particle volume fraction shown in Fig. 7. The range of values represented in the figure is very limited, and averaging to eliminate noise runs the serious risk of destroying much of the signal as well. This danger would be even greater at larger volume fractions, in which the fluctuations around the mean would be even smaller.

These difficulties have prompted us to develop a different way to interrogate the results of our simulations by relying on the use of a truncated Fourier series to coarse-grain the fields obtained from the resolved simulations.

V. FOURIER RECONSTRUCTION

The numerical simulations furnish what may be called "microscopic" information on the various quantities characterizing the process under consideration. For the particle number density such
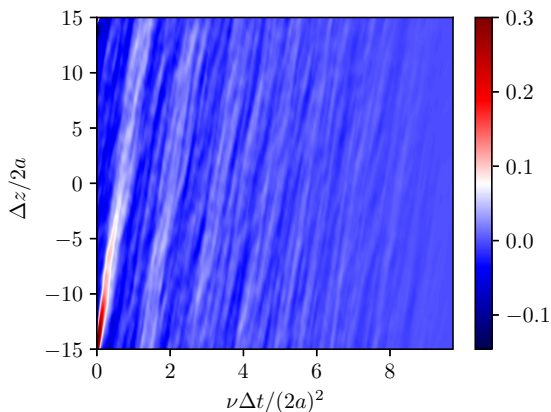

FIG. 6. Autocorrelation of the "raw" particle volume fraction ϕ (i.e., the particle volume fraction obtained by counting the fraction of volume of each horizontal cell layer falling inside particles) for $\rho_p/\rho = 3.3$ with 1000 particles; the quantity shown is averaged over z and t.
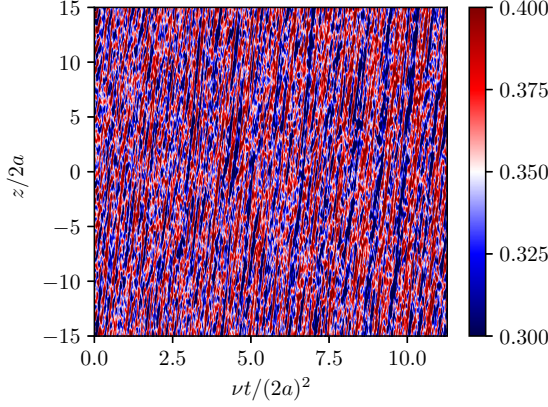
FIG. 7. Space-time distribution of the "raw" particle volume fraction (i.e., the particle volume fraction obtained by counting the fraction of volume of each horizontal cell layer falling inside particles) for $\rho_p/\rho = 3.3$ with 2000 particles.

microscopic information is embodied in a field n_{micr} defined by

$$n_{\text{micr}}(\mathbf{x},t) = \sum_{\alpha=1}^{N_p} \delta[\mathbf{x} - \mathbf{x}^{\alpha}(t)], \tag{9}$$

where $\mathbf{x}^{\alpha}(t)$ is the instantaneous position of the center of the αth particle and N_p the total number of particles. This quantity can be expanded in a Fourier series as

$$n_{\text{micr}}(\mathbf{x},t) = \sum_{\mathbf{k}} n(\mathbf{k},t) \exp(i\mathbf{k} \cdot \mathbf{x}), \tag{10}$$

where the summation ranges over all the wave vectors $\mathbf{k} = 2\pi(n/L_x, m/L_y, \ell/L_z)$ in the reciprocal lattice; L_x, L_y, and L_z are the dimensions of the computational domain in the three coordinate directions and ℓ, m, and n integers. The Fourier coefficients $n(\mathbf{k},t)$ are given by the scalar products

$$n(\mathbf{k},t) = \frac{1}{V}(\exp[i\mathbf{k} \cdot \mathbf{x}], n_{\text{micr}}) = \frac{1}{V} \sum_{\alpha=1}^{N_p} \exp[-i\mathbf{k} \cdot \mathbf{x}^{\alpha}(t)], \tag{11}$$

with $V = L_x L_y L_z$ the volume of the computational domain.

Retention of the infinite number of terms in the Fourier expansion (10) would reproduce n_{micr}, but a suitable truncation of the series will generate a coarse-grained version of n_{micr}. Furthermore, retaining only the terms of the series with wave numbers $\mathbf{k}$ parallel to the z axis is equivalent to averaging over horizontal planes. On the basis of these considerations we define the coarse-grained number density as

$$n(z,t) = \sum_{\ell=-N}^{N} n_{\ell}(t) \exp(ik_{\ell}z), \tag{12}$$

with $k_{\ell} = 2\pi\ell/L_z$ and

$$n_{\ell}(t) = \frac{1}{V} \sum_{\alpha=1}^{N_p} \exp[-ik_{\ell}z^{\alpha}(t)]. \tag{13}$$

A suitable value for N can be estimated by recognizing that the smallest features of the coarse-grained number density field n that it makes sense to consider in a macroscopic framework should not be

so small as to permit the identification of single particles. If we choose this shortest wavelength to be two particle diameters, we have $N = L_z/(4a) = 15$, and we find the result shown by the solid line in Fig. 3. While this is just an estimate, we have found that the results are not very different if this number is increased up to 30 or decreased to 10, which would amount to include wavelengths as short as the particle diameter or as long as three diameters, respectively. As an example, the thick dashed line in Fig. 3 shows the particle number density reconstructed with 30 terms. Some more detail can be identified in this line, but the 15-term reconstruction overall reproduces well the large-scale (and, therefore, properly macroscopic) features of the number density.

We can deal in a similar way with any other quantity associated with the particles. In particular, the microscopic version of the volume fraction, ϕ_{micr}, equal to one inside the particles and zero in the fluid, can be expressed as

$$\phi_{\text{micr}}(\mathbf{x},t) = \sum_{\alpha=1}^{N_p} H[a - |\mathbf{x} - \mathbf{x}_\alpha(t)|], \tag{14}$$

with H the Heaviside step function. Its Fourier-series expansion is

$$\phi_{\text{micr}}(\mathbf{x},t) = \sum_{\mathbf{k}} \phi(\mathbf{k},t) \exp(i\mathbf{k} \cdot \mathbf{x}), \tag{15}$$

with

$$\phi(\mathbf{k},t) = \frac{1}{V}(\exp[i\mathbf{k} \cdot \mathbf{x}], \phi_{\text{micr}}) = \frac{1}{V} \sum_{\alpha=1}^{N_p} \int_{v^\alpha} \exp[-i\mathbf{k} \cdot \mathbf{x}] H[a - |\mathbf{x} - \mathbf{x}_\alpha(t)|] \, dv^\alpha$$

$$= \frac{4\pi}{k^3} (\sin ka - ka \, \cos ka) n(\mathbf{k},t). \tag{16}$$

Here each integral in the first line is extended over the volume v^α of the αth particle and $k = |\mathbf{k}|$. It is worth noting that the last step shown here is a direct consequence of the expression for the Fourier coefficients and could not be obtained in a volume averaging context.

Again, we obtain a horizontally averaged coarse-grained volume fraction field by considering only the coefficients of order 0 in the horizontal directions and truncating the sum:

$$\phi(z,t) = \sum_{\ell=-N}^{N} \phi_\ell(t) \exp(ik_\ell z). \tag{17}$$

This is the coarse-grained version of ϕ_{micr} which we identify with the ϕ appearing in the macroscopic theory. Since ϕ_{micr} is highly discontinuous, in order to avoid possible convergence problems caused by the Gibbs phenomenon, the sum in Eq. (17) is calculated according to the Cesáro summation method [34].

An example of the spatio-temporal representation of the field ϕ obtained in this way is shown in Fig. 8. In spite of the statistical noise, the wave structure of the particle distribution is much clearer than in Fig. 7.

A. The speed of kinematic waves

The autocorrelation of the particle volume fraction reconstructed with 15 Fourier coefficients and averaged over z and t is shown in Fig. 9. The wave structure of the particle distribution is strikingly clearer than in Figs. 6 and 4. In order to calculate the wave speed from these results, for each value of Δz we find the Δt corresponding to the first maximum, form the ratio $\Delta z/\Delta t$ and then average the results obtained in this way. The standard deviation of the distribution of values of $\Delta z/\Delta t$ about this average permits us to estimate the error of this determination. The results obtained in this way are shown in Fig. 10. The lines shown in the figure are graphs of the average-equation result (7) constructed with the values of w_t, n, and κ calculated in this work and shown in Tables II and III.
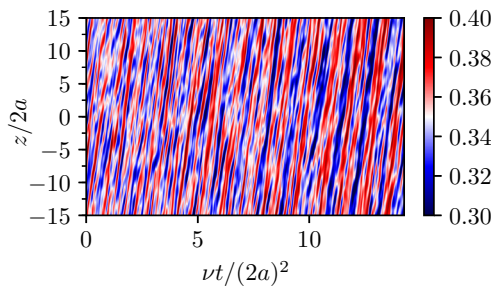
FIG. 8. Fifteen-terms Fourier reconstruction of the volume fraction for a representative case with $\phi = 0.349$ ($N = 2000$) and $\rho^* = 3.3$; white corresponds to the mean volume fraction over the entire computational domain. This figure should be compared with Fig. 7 in which the "raw," rather than the Fourier-processed, volume fraction is shown.

Overall, the agreement between (7) and the numerical results is very good. Accounting for the confidence levels of the fits shown in Fig. 1 brings the lines within the expected range of the computational results for all but the lowest volume fraction points, where a discrepancy of less than 5% remains. A possible explanation is that, at low volume fractions, the mean-free path of the particles is long enough that dynamic effects become significant and the kinematic wave model therefore less applicable. For the larger density ratios and volume fractions the completion of all the necessary simulations would have required more time than seemed warranted by the very good agreement between macroscopic theory and simulations displayed in the figure; we have chosen to proceed without including these results.

B. The fluid velocity field

A similar procedure can be adopted for the fields of the continuous phase. We consider the fluid velocity field in the vertical direction, $w_f(z,t)$ and write its coarse-grained version by truncating its Fourier series expansion:

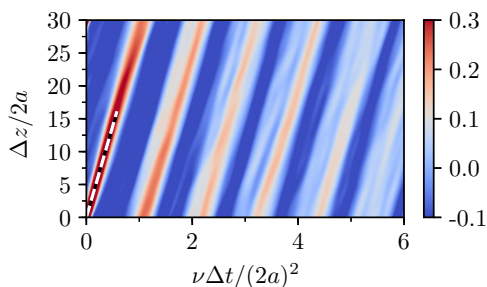$$\phi(z,t)w_f(z,t) = \sum_{\ell=-N}^{N} w_\ell(t) \exp(ik_\ell z), \qquad (18)$$

FIG. 9. Autocorrelation of the particle volume fraction reconstructed with 15 Fourier terms for a representative case with $\phi = 0.349$ ($N = 2000$) and $\rho^* = 3.3$. The dashed line is obtained by a least-squares fit of the position of the maxima for each Δz. This figure may be compared with Figs. 6 and 4 which show the autocorrelation of the "raw" volume fraction and number density, respectively.
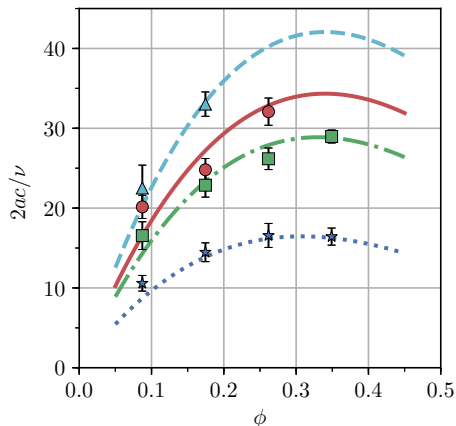
FIG. 10. Continuity wave speed calculated from the present simulations (symbols) compared to the relationship given in Eq. (7) shown by the dashed lines.

with

$$w_\ell(t) = \frac{1}{V} \int_V w_f(\mathbf{x},t)\chi_f(\mathbf{x},t)\exp(ik_\ell z)\,dV, \tag{19}$$

where $\chi_f(\mathbf{x},t)$ is the indicator function of the fluid phase and the integral is over the entire volume of the computational domain. A useful feature of this approach is that the volume occupied by the particles is excluded in a natural way.

The relation between the instantaneous velocities calculated with this truncated Fourier series reconstruction with $N = 15$ and by averaging over horizontal cell layers is shown by the solid and dashed lines, respectively, in Fig. 11. The effectiveness of the Fourier method to remove noise is particularly evident here.

The presence of kinematic waves can be detected in the fluid velocity autocorrelation in the same way demonstrated before. An example is shown in Fig. 12. The picture is somewhat fuzzier than for the volume fraction, but the dashed line with the slope as calculated by a least square method as explained before provides a good fit to the velocity maxima. The dimensionless slope corresponding to this line is $2ac/\nu = 21.37$, which differs by about 7% from the value 22.86 shown in Fig. 10.
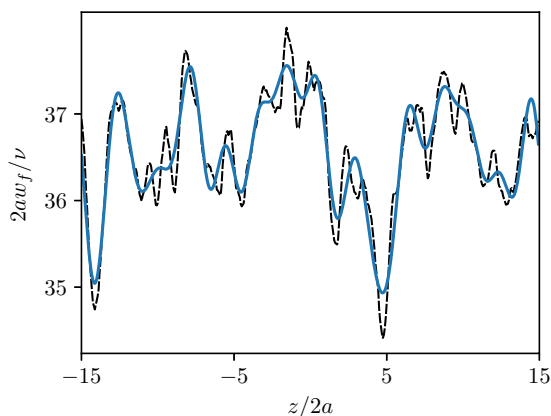

FIG. 11. Instantaneous fluid vertical velocity vs. z as calculated from the Fourier reconstruction with $N = 15$ coefficients (solid line) and by averaging over horizontal cell layers for $\rho_p/\rho = 3.3$ with 1000 particles.
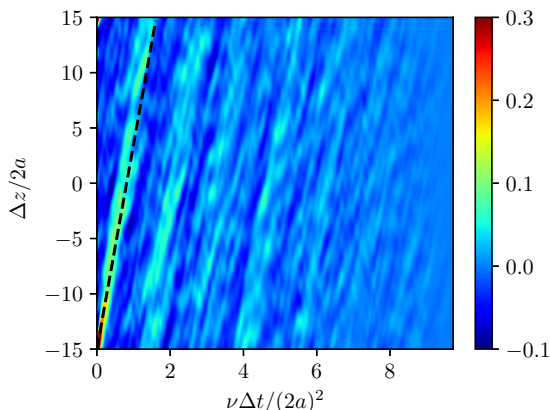
FIG. 12. Autocorrelation function of the "raw" fluid vertical velocity, i.e., the fluid vertical velocity averaged over each horizontal cell layer; the quantity shown is averaged over z and t for $\rho_p/\rho = 3.3$ and 1000 particles.

On intuitive grounds it may be expected that fluid velocity and particle volume fraction would be oppositely correlated so that a graph of the cross-correlation function

$$R_{w\phi}(\Delta z, \Delta t) = \frac{\langle [w_f(z + \Delta z, t + \Delta t) - \langle w_f \rangle] [\phi(z,t) - \langle \phi \rangle] \rangle}{\sqrt{\sigma_w \sigma_\phi}}, \quad (20)$$

should exhibit a pronounced negative minimum along lines $\Delta z = c(\Delta t + NT)$. This expectation is indeed borne out by the results of Fig. 13, where the line has the slope $2ac/\nu = 21.37$.

C. Power spectra

The squares of the Fourier coefficients plotted as functions of the wave number give directly the power spectra of the waves. These spectra, calculated from the Fourier-reconstructed volume fraction, are shown in Fig. 14 for all the parameter values simulated in this work as functions of L_z/λ_ℓ, with $\lambda_\ell = 2\pi/k_\ell$. In each case the spectra are normalized by the maximum value.
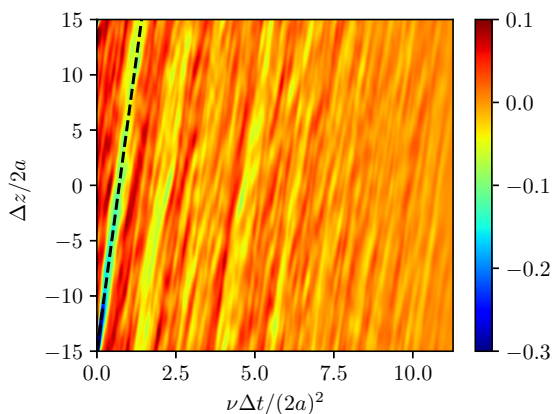

FIG. 13. Normalized cross-correlation of volume fraction and fluid vertical velocity, each reconstructed with 15 Fourier modes, for the case $\rho_p/\rho = 3.3$ with 1000 particles. The slope of the dashed line is the speed of kinematic waves calculated from the reconstructed volume fraction as explained in the text.
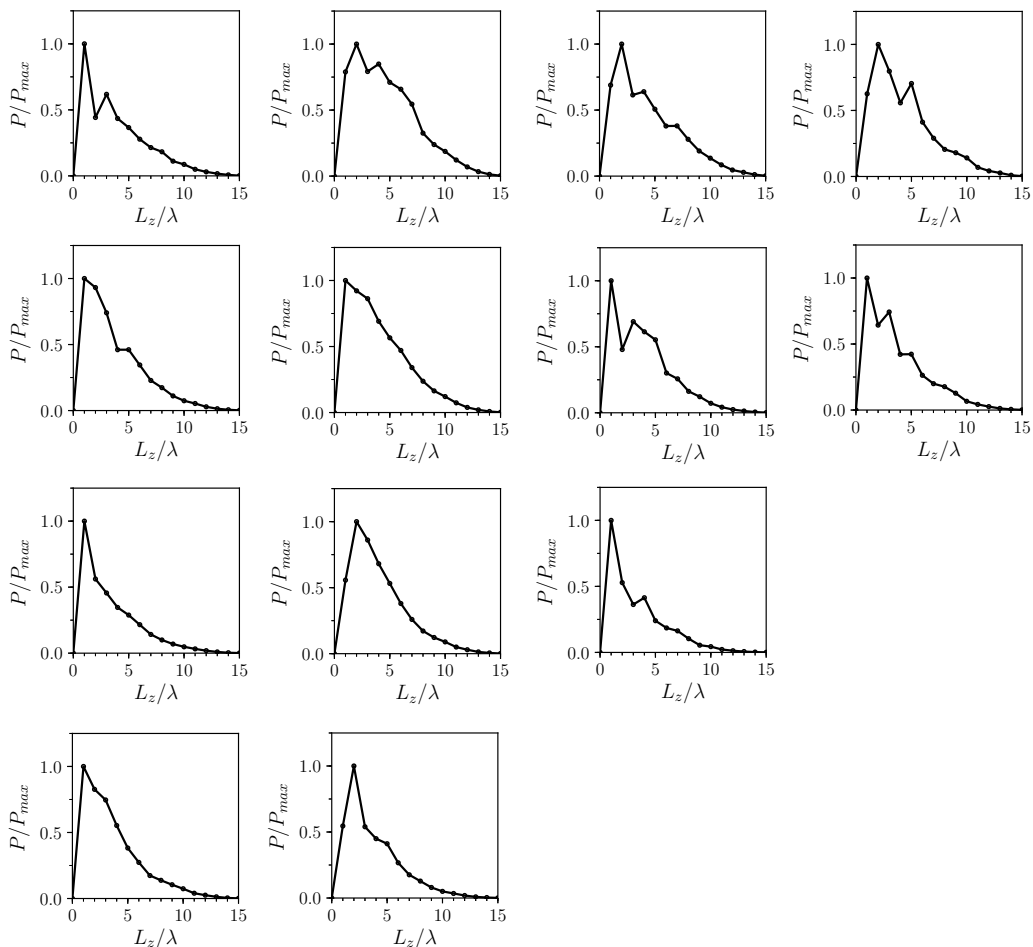
FIG. 14. Spatial power spectra of the Fourier-reconstructed volume fraction; λ denotes the wavelength of the Fourier components. From left to right, the columns correspond to $\phi = 0.087, 0.175, 0.262, 0.349$; from top to bottom the rows are for $\rho_p/\rho = 2, 3.3, 4$, and 5.

Several spectra exhibit a dominant peak for a wavelength equal to half the height of the computational domain, while in other cases the dominant peak is for a wavelength equal to the height of the domain. This is an indication that, in these latter cases, the computational domain used is too short to include the entire wave. Nevertheless, since the wave speed is independent of the wavelength as noted after (7), the present results for the wave speed are unaffected by this limitation. Indeed, upon comparing with the graph of the wave speeds in Fig. 10, it is seen that velocities corresponding to cases with peaks at $\lambda = L_z$ and $\lambda = \frac{1}{2}L_z$ exhibit a comparable agreement with the kinematic wave theory.

A comparison between the spectra calculated from the Fourier-reconstructed fluid velocity and volume fraction is shown for one case in Fig. 15. The two spectra are quite similar as expected.

The temporal spectra can be found by expanding the Fourier-reconstructed signal (e.g., the volume fraction) in a Fourier series in time at each spatial point and then averaging over space. An example of the results obtained in this way is shown in Fig. 16 for $\rho_p/\rho = 3.3$ and 1000 particles. The two nearly superposed lines are the results found from the reconstructed volume fraction and vertical fluid velocity. There is a prominent peak at $f_* \equiv (2a)^2 f/\nu \simeq 0.71$. Forming the product $(\lambda/2a) f_* = 2ac/\nu$ with $\lambda = L_z$ we find $2ac/\nu \simeq 21.3$, to be compared with the value 22.86 from
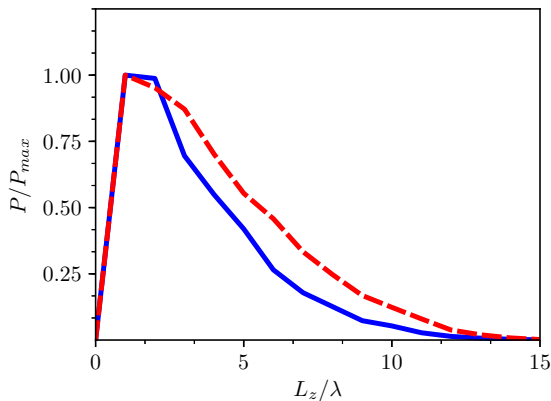
FIG. 15. Power spectra of the particle volume fraction (solid line) and of the fluid vertical velocity, both reconstructed with 15 Fourier coefficients, vs the normalized wave number for $\rho_p/\rho = 3.3$ with 1000 particles.

Fig. 10. The difference between the two values is likely due to the need to omit, in the calculation of the spectrum, data corresponding to the initial transient, the end of which is somewhat ill-defined. We have found that the position of the peak frequency moves slightly as the fraction of omitted data is changed. Figure 16 also exhibits another strong peak at the first harmonic $f_* \simeq 1.5$, another much weaker one at the second harmonic $f_* \simeq 2$ and other smaller ones as well.

VI. DISCUSSION AND CONCLUSION

In this paper we have demonstrated a method to extract average properties from the results of direct numerical simulations of particulate flows. We have used the method to reconstruct the coarse-grained volume fraction and fluid velocity field in the fully resolved simulation of a fluidized-bedlike system in which equal spheres are suspended in an upward flow of a fluid with comparable, but smaller, density. In particular, we have shown that the coarse-grained fields show the presence of kinematic waves propagating upward in the bed. The celerity of these waves is very close to that produced by existing macroscopic description of such systems.

Reference [18] describes a study of volume fraction waves forced by the oscillations of the distributor at the bottom of a liquid-filled tube for particles with a density ratio comparable to the
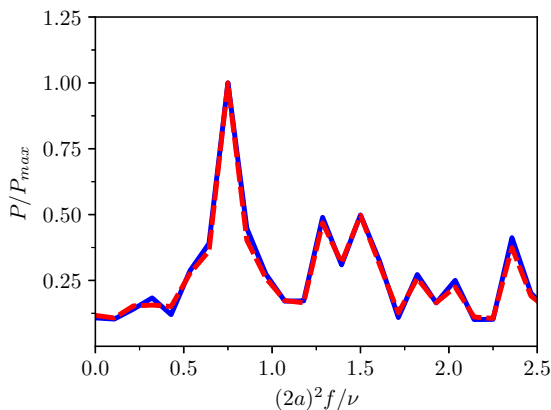

FIG. 16. Power spectra of the particle volume fraction (solid line) and of the fluid vertical velocity, both reconstructed with 15 Fourier coefficients, vs the normalized frequency, for $\rho_p/\rho = 3.3$ with 1000 particles.

present one and a Galileo number slightly larger than ours. In the volume fraction range of our simulations they characterize their observations as "turbulent regime" and were unable to identify clear wavelike structures by their method. A visual inspection of the particle motion computed in this work (see the video uploaded with the Supplemental Material [35], which refers to 2000 particles with $\rho^* = 3.3$) confirms this disorderly appearance. Nevertheless, in spite of their convoluted appearance, the volume fraction iso-surfaces given by the filtered three-dimensional Fourier reconstruction, shown on the right, convey the clear impression of upward moving structures. These wave emerge therefore as a very robust feature of the dynamics of the system investigated in spite of the complex horizontal structure of the numerical results as well as, in all likelihood, of experiment.

ACKNOWLEDGMENTS

---

[1] G. Whitham, *Linear and Nonlinear Waves* (Wiley, New York, NY, 1974).

[2] G. Wallis, *One Dimensional Two-Phase Flow* (McGraw-Hill, New York, NY, 1969).

[3] R. Jackson, *The Dynamics of Fluidized Particles* (Cambridge University Press, Cambridge, UK, 2000).

[4] T. Anderson and R. Jackson, A fluid mechanical description of fluidized beds: Comparison of theory and experiment, Ind. Eng. Chem. Fund. **8**, 137 (1969).

[5] M. El-Kaissy and G. Homsy, Instability waves and the origin of bubbles in fluidized beds: Part I: Experiments, Int. J. Multiphase Flow **2**, 379 (1976).

[6] A. Didwania and G. Homsy, Flow regimes and flow transitions in liquid fluidized beds, Int. J. Multiphase Flow **7**, 563 (1981).

[7] P. Duru and E. Guazzelli, Experimental investigation on the secondary instability of liquid-fluidized beds and the formation of bubbles, J. Fluid Mech. **470**, 359 (2002).

[8] G. Batchelor, A new theory of the instability of a uniform bed, J. Fluid Mech. **193**, 75 (1988).

[9] G. Batchelor, Secondary instability of a gas-fluidized bed, J. Fluid Mech. **257**, 357 (1993).

[10] K. Anderson, S. Sundaresan, and R. Jackson, Instabilities and the formation of bubbles in fluidized beds, J. Fluid Mech. **303**, 327 (1995).

[11] M. Göz, Transverse instability of plane voidage wavetrains in gas-fluidized beds, J. Fluid Mech. **303**, 55 (1995).

[12] B. Glasser, I. Kevrekidis, and S. Sundaresan, One- and two-dimensional traveling wave solutions in gas-fluidized beds, J. Fluid Mech **306**, 183 (1996).

[13] B. Glasser, I. Kevrekidis, and S. Sundaresan, Fully developed traveling wave solutions and bubble formation in fluidized beds, J. Fluid Mech **334**, 157 (1997).

[14] S. Sundaresan, Instabilites in fluidized beds, Ann. Rev. Fluid Mech. **35**, 63 (2003).

[15] G. Kynch, A theory of sedimentation, Trans. Faraday Soc. **48**, 166 (1952).

[16] P. Slis, T. Willemse, and H. Kramers, The response of the level of a liquid fluidized bed to a sudden change in the fluidization velocity, Appl. Sci. Res., Ser. A **8**, 209 (1959).

[17] J. Derksen and S. Sundaresan, Direct numerical simulations of dense suspensions: Wave instabilities in liquid-fluidized beds, J. Fluid Mech. **587**, 303 (2007).

[18] P. Duru, M. Nicolas, J. Hinch, and E. Guazzelli, Constitutive laws in liquid-fluidized beds, J. Fluid Mech. **452**, 371 (2002).

[19] A. J. Sierakowski and A. Prosperetti, Resolved-particle simulation by the Physalis method: Enhancements and new capabilities, J. Comput. Phys. **309**, 164 (2016).

[20] A. J. Sierakowski, Gpu-centric resolved-particle disperse two-phase flow simulation using the Physalis method, Phys. Commun. **207**, 24 (2016).

[21] H. Lamb, *Hydrodynamics* (Cambridge UP, Cambridge, UK; reprinted by Dover, New York, NY, 1932).

[22] S. Kim and S. Karrila, *Microhydrodynamics: Principles and Selected Applications* (Butterworth-Heinemann, Boston, MA; reprinted by Dover, New York, NY, 1991).

[23] K. Gudmundsson and A. Prosperetti, Improved procedure for the computation of Lamb's coefficients in the Physalis method for particle simulation, J. Comput. Phys. **234**, 44 (2013).

[24] J. Richardson and W. Zaki, Sedimentation and fluidisation: Part I, Trans. Inst. Chem. Eng. **32**, 35 (1954).

[25] G. Barnocky and R. Davis, Elastohydrodynamic collision and rebound of spheres: Experimental verification, Phys. Fluids **31**, 1324 (1988).

[26] X. Yin and D. Koch, Hindered settling velocity and microstructure in suspensions of solid spheres with moderate Reynolds numbers, Phys. Fluids **19**, 093302 (2007).

[27] J. Garside and M. Al-Dibouni, Velocity-voidage relationships for fluidization and sedimentation in solid-liquid systems, Ind. Eng. Chem., Process Des. Dev. **16**, 206 (1977).

[28] Y. Chong, D. Ratkowsky, and N. Epstein, Effect of particle shape on hindered settling in creeping flow, Powder Technol. **23**, 55 (1979).

[29] R. di Felice and E. Parodi, Wall effects on the sedimentation velocity of suspensions in viscous flow, AlChE J. **42**, 927 (1996).

[30] R. di Felice, The sedimentation velocity of dilute suspensions of nearly monosized spheres, Int. J. Multiphase Flow **25**, 559 (1999).

[31] E. Barnea and J. Mizrahi, A generalized approach to the fluid dynamics of particulate systems: Part 1: General correlation for fluidization and sedimentation in solid multiparticle systems, Chem. Eng. J. **5**, 171 (1973).

[32] L. van Wijngaarden and C. Kepteyn, Concentration waves in dilute bubble/liquid mixtures, J. Fluid Mech. **212**, 111 (1990).

[33] R. Zenit, D. Koch, and A. Sangani, Measurements of the average properties of a suspension of bubbles rising in a vertical channel, J. Fluid Mech. **429**, 307 (2001).

[34] C. Canuto, M. Hussaini, A. Quarteroni, and T. Zang, *Spectral Methods: Fundamentals in Single Domains* (Springer, Berlin, 2006).

[35] See Supplemental Material at http://link.aps.org/supplemental/10.1103/PhysRevFluids.2.114305 for a movie with two parallel sequences. The one on the left shows the results of the simulation; the sequence on the right shows the volume-fraction iso-surfaces corresponding to volume factions lower (blue) and higher (red) than the average, obtained with a Fourier reconstruction including 15 terms in the vertical direction and 5 terms in each one of the horizontal directions. The simulations are for 1000 particles with a density ratio of 3.3.